PAPER

Exploring the crystal structure and properties of ytterbium orthoantimonate under high pressure†

Alka B. Garg,[a,b] Sinhue Lopez-Moreno, [ID][c,d] Pablo Botella-Vives, [ID][e] Oscar Gomis, [ID][f] Enrico Bandiello, [ID][g] Hussien Osman,[e,g] Catalin Popescu [ID][h] and Daniel Errandonea [ID]*[e]

The crystal structure of $YbSbO_4$ was determined from powder X-ray diffraction data using the Rietveld method. $YbSbO_4$ is found to be monoclinic and isostructural to α-$PrSbO_4$. We have also tested the influence of pressure on the crystal structure up to 22 GPa by synchrotron powder X-ray diffraction. No phase transition was found. The P–V equation of state and axial compressibilities were determined. Experiments were combined with density-functional theory calculations, which provided information on the elastic constants and the influence of pressure in the crystal structure and Raman/infrared phonons. Results are compared with those from other orthoantimonates. Reasons for the difference in the high-pressure behaviour of $YbSbO_4$ compared with most antimony oxides will be discussed.

1. Introduction

The high-pressure (HP) behaviour of MTO_4 bimetal oxides has been the focus of research interest during the last two decades.[1,2] The main objects of study have been phosphates,[3,4] vanadates,[5,6] tungstates,[7,8] molybdates,[9,10] chromates,[11,12] niobates,[13,14] and tantalates.[15,16] On the other hand, a group of compounds that have been barely studied under HP are orthoantimonates, among which only $BiSbO_4$ has been studied.[17] Contrary to the rest of the MTO_4 compounds, this material shows a surprising structural stability under HP, not undergoing any phase transition up to 70 GPa, the maximum pressure reached by studies. Therefore, it is important to study other antimonate compounds under HP to understand the effect of pressure on their properties.

Among antimonates, lanthanide antimonates are technologically important compounds.[18] Their rich luminescent properties have been proposed for applications such as laser materials, flat panel displays, cathode ray tubes, up-conversion devices, and white light-emitting diodes.[18] The understanding of their fundamental physical properties is of importance for these and other technological applications. It is a very well-known fact that HP modifies interatomic bonds, triggering changes in the structural, physical, and chemical properties of materials.[19] Consequently, HP research has made relevant contributions to the understanding of the properties of materials, and consequently to the progress of materials science.[20]

In order to deepen the knowledge of the properties and HP behaviour of lanthanide antimonates, we have performed a study on ytterbium orthoantimonate ($YbSbO_4$). We have studied it by combining HP X-ray diffraction (XRD) measurements and density-functional theory (DFT) calculations. The crystal structure, its behaviour under HP, and the vibrational and elastic properties will be reported, discussed, and compared with related compounds.

[a]*High Pressure and Synchrotron Radiation Physics Division, Bhabha Atomic Research Centre, Mumbai 400085, India*

[b]*Homi Bhabha National Institute, Anushaktinagar, Mumbai 400094, India*

[c]*CONAHCYT—División de Materiales Avanzados, IPICYT, Camino a la presa de San José 2055 Col. Lomas 4a sección, San Luis Potosí 78126, Mexico*

[d]*Centro Nacional de Supercómputo, IPICYT, Camino a la presa de San José 2055 Col. Lomas 4a sección, San Luis Potosí 78126, Mexico*

[e]*Departamento de Física Aplicada, Instituto de Ciencias de Materiales, MALTA Consolider Team, Universidad de Valencia, 46100 Valencia, Spain. E-mail: daniel.errandonea@uv.es*

[f]*Centro de Tecnologías Físicas: Acústica, Materiales y Astrofísica, MALTA Consolider Team, Universitat Politècnica de València, 46022 Valencia, Spain*

[g]*Instituto de Diseño para la Fabricación y Producción Automatizada, MALTA Consolider Team, Universitat Politècnica de València, 46022 Valencia, Spain*

[h]*CELLS–ALBA Synchrotron Light Facility, Cerdanyola del Valles E-08290, Barcelona, Spain*

†Electronic supplementary information (ESI) available. See DOI: https://doi.org/10.1039/d3dt02480f

2. Materials and methods

Polycrystalline $YbSbO_4$ was synthesized through a solid-state reaction following the procedure described by Siqueira *et al.*[18] The synthesis was made using a stoichiometric mixture of high-purity Yb_2O_3 (>99.9% Sigma-Aldrich) and high-purity Sb_2O_5 (>99.9% Sigma-Aldrich), the starting materials were

mixed with a mortar and pestle and subsequently calcined with intermediate regrinding until obtaining a single-phase compound. The composition of the material was verified by scanning electron microscopy (SEM) and Energy-dispersive X-ray analysis (EDX) using a Hitachi S-4800 high-resolution scanning electron microscope, using an accelerating voltage of 30 kV. Ambient pressure structural characterization and phase identification were performed by powder XRD with a Rigaku D/max diffractometer using a Bragg–Brentano geometry and monochromatic Cu-K$_{\alpha 1}$ radiation.

Room-temperature HP powder XRD experiments were performed at the BL04-MSPD beamline of the ALBA synchrotron.[21] We used a diamond-anvil cell (DAC) with culets of 500 μm in diameter and an Inconel gasket. A 250 μm diameter hole drilled in the center of the gasket served as the pressure chamber. We used a 16 : 3 : 1 methanol–ethanol–water mixture as a pressure medium[22] and XRD of Cu as the pressure scale.[23] We employed a monochromatic X-ray beam (λ = 0.4642 Å) focused to 20 μm × 20 μm (full-width-at-half-maximum) and collimated with a molybdenum pinhole and a two-dimensional Rayonix SX165 CCD detector. The two-dimensional diffraction images were transformed into conventional XRD patterns using DIOPTAS.[24] Rietveld refinements were performed with FullProf.[25]

Total-energy calculations were performed within the framework of DFT[26] using the projector-augmented wave method[27,28] as implemented in the Vienna *Ab initio* Simulation Package (VASP).[29] We used a plane-wave energy cutoff of 520 eV ensuring high precision in our calculations. The exchange–correlation energy was described within the generalized-gradient approximation (GGA) in the Perdew–Burke–Ernzerhof for solids (PBEsol) formulation.[30] The Monkhorst–Pack scheme was employed for the Brillouin-zone (BZ) integrations[31] with a mesh 3 × 4 × 3 which corresponds to a set of ten special *k*-points in the irreducible BZ for the conventional unit cell. In the relaxed equilibrium configuration, the forces are less than 0.3 meV per Å per atom in each cartesian direction. The highly converged results on forces are required for the calculations of the dynamical matrix using the direct force constant approach.[32] This allows us to identify the irreducible representation and the character of the phonon modes at the zone center (Γ point). The phonon density of states (PDOS) has been obtained calculating the phonon spectrum in the whole BZ with a supercell 2 × 2 × 2 times the conventional unit cell using the PHONON software.[32] We computed the elastic constants with a 6 × 8 × 6 *k*-points mesh with the unit cell, a plane-wave energy cut-off of 570 eV, and a POTIM parameter of 0.016. The elastic tensor is determined by performing six finite lattice distortions and deriving the elastic constants from the strain–stress relationship.[33]

3.   Results and discussion

A SEM image of our sample is shown in Fig. 1(a). In the figure we highlight the five areas where we collected EDX to study the
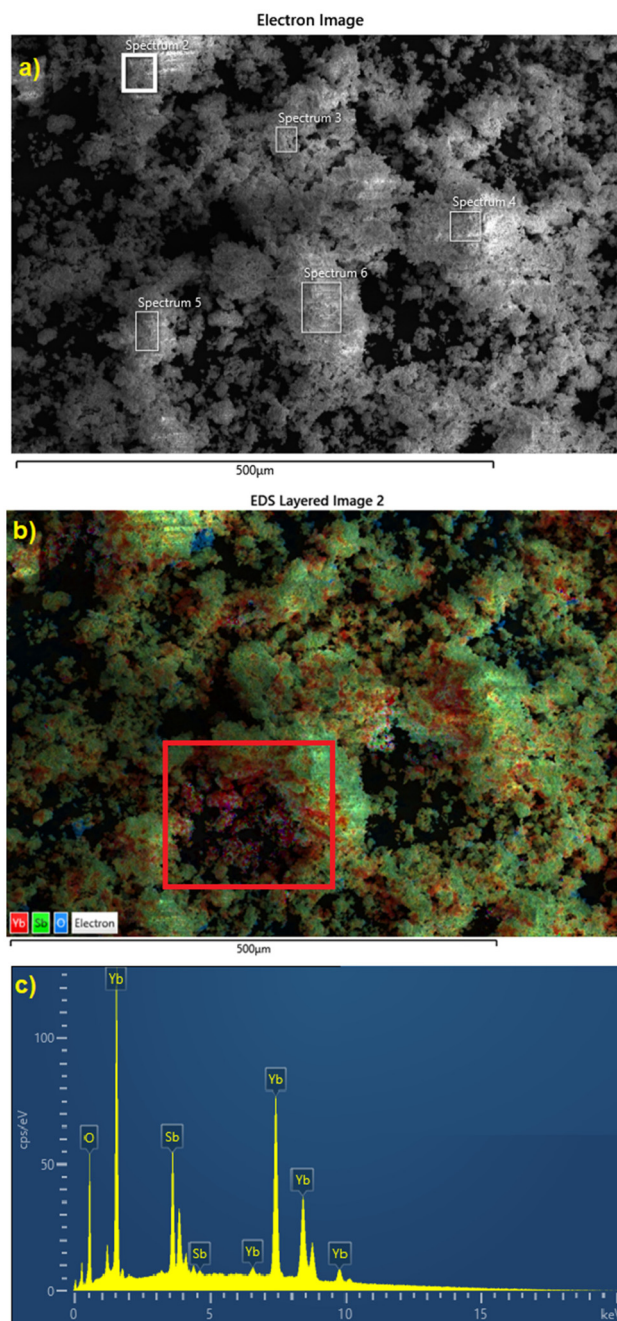

Fig. 1 (a) Scanning electron microscopy of the YbSbO$_4$ powder showing five areas where EDX was collected. (b) A zoom of area labeled as spectrum 2 in (a) showing color images. The red rectangle shown an area with excess of Yb. (c) EDX spectrum.

composition of the sample. Fig. 1(b) shows a SEM color image of one of these areas. A region where an excess of Yb was detected is highlighted within a red rectangle. From EDX (Fig. 1(c)), we determined that the molar ratio of Yb and Sb in the synthesized sample is close to 1 : 1 (Yb 51.2 at% and Sb 48.8 at%) confirming the slight Yb excess.

In Fig. 2(a) we present the powder XRD pattern of YbSbO$_4$ as measured at ambient conditions. Only a single phase was
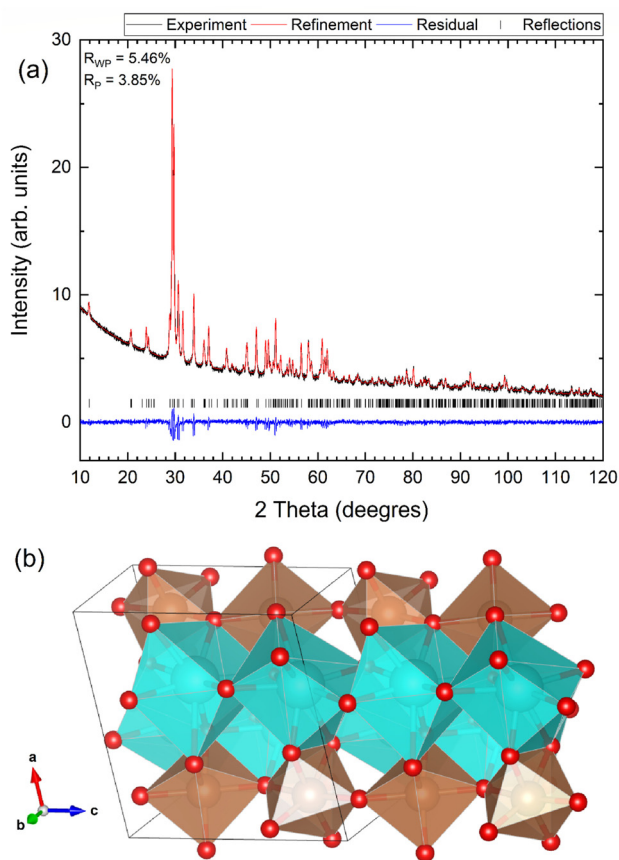
Fig. 2 (a) XRD pattern of $YbSbO_4$ as measured at ambient conditions. (b) Crystal structure of $YbSbO_4$. The Sb and Yb coordination polyhedra are shown in brown and cyan, respectively.

Table 1 Experimental unit-cell parameters, atomic positions, and bond-distances of $YbSbO_4$ at ambient pressure

$a = 7.5096(8)$ Å, $b = 5.2883(5)$ Å, $c = 7.4002(7)$ Å, and $\beta = 98.978(9)°$

Atom	Site	x	y	z
Yb	4e	0.35620(3)	0.21570(2)	0.10970(1)
Sb	4e	0.15270(2)	0.72220(4)	0.30550(4)
O_1	4e	0.0728(4)	0.1128(4)	0.6943(5)
O_2	4e	0.1611(4)	0.6199(5)	0.5625(5)
O_3	4e	0.3294(4)	0.5096(5)	0.8799(6)
O_4	4e	0.3793(4)	0.5424(5)	0.3290(4)

$Sb-O_1 = 1.905(7)$ Å, $Sb-O_4 = 1.933(7)$ Å, $Sb-O_3 = 1.962(6)$ Å, $Sb-O_2 = 1.969(7)$ Å, $Sb-O_2 = 1.993(7)$ Å, and $Sb-O_1 = 2.005(6)$ Å. $Yb-O_4 = 2.170(7)$ Å, $Yb-O_3 = 2.289(6)$ Å, $Yb-O_2 = 2.293(6)$ Å, $Yb-O_4 = 2.358(6)$ Å, $Yb-O_3 = 2.363(7)$ Å, $Yb-O_1 = 2.482(7)$ Å, $Yb-O_4 = 2.514(7)$ Å, and $Yb-O_3 = 2.763(7)$ Å.

In Fig. 3 we report a selection of HP XRD patterns at different pressure points. We have found that all of these patterns can be identified with a crystal structure isomorphic to

observed. However, as we will comment when discussing the HP experiments, synchrotron powder XRD detected and small amount of Yb_2O_3 impurities, which agrees with the Yb excess detected by EDX. A possible reason for it is the known fact that Sb_2O_5 has a sublimation tendency due to formation Sb_2O_{5-x} species.[34] The XRD pattern was Rietveld refined assuming as model the structure of α-$PrSbO_4$,[35] leading to small R-values (see Fig. 2(a)), indicating a good fit of the structural model to the data. The crystal structure including atomic positions is here reported for the first time. In ref. 18, the same kind of crystal structure was proposed, but only rough lattice parameters a, b, and c were reported in a figure, being numerical values not provided. The crystal structure is monoclinic (space group $P2_1/c$) and it is represented in Fig. 2(b), while the structural information is given in Table 1. The cif file is included in the ESI† and has been uploaded to the Cambridge Crystallographic Data Centre (Deposition number 2293383†). The structure can be visualized as chains of nearly regular corner-sharing SbO_6 octahedra which run parallel to chains of high-distorted edge-sharing YbO_8 dodecahedra, which also share edges with adjacent SbO_6 octahedra. Bond distances are also provided in Table 1. The average Sb–O bond length is 1.961(7) Å (the standard deviation is 0.035 Å) and the average Yb–O bond length is 2.404(7) Å (the standard deviation is 0.181 Å).
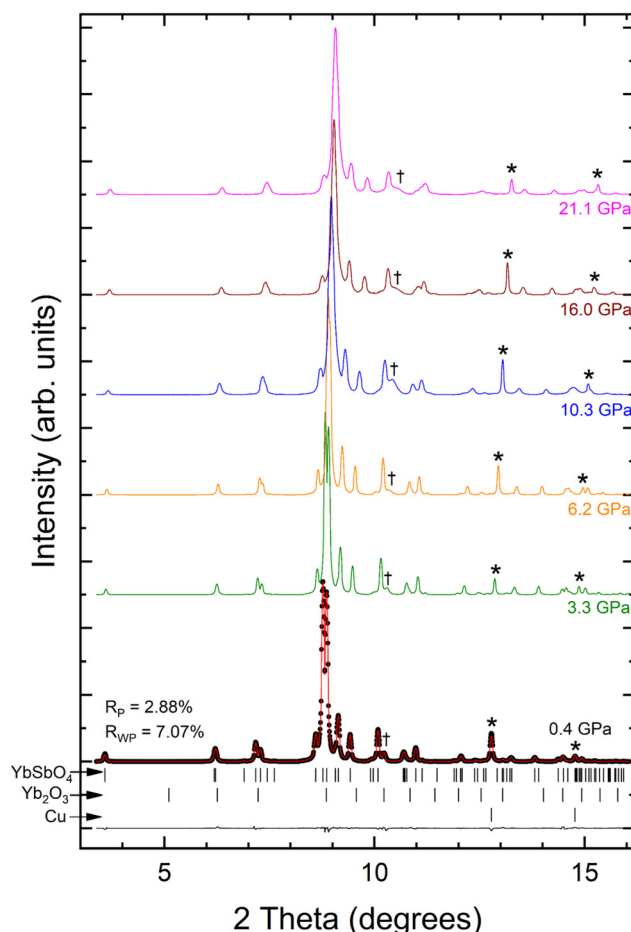

Fig. 3 HP XRD patterns measured at different pressure. In the pattern at the lowest pressure the experiment (refinement) is shown with black circles (red line). The black line is the residual and the vertical ticks shown the position of Bragg peaks. Asterisks identify peaks of Cu (pressure marker) and the dagger symbols the most intense peaks of the Yb_2O_3 minority phase.

that of the low-pressure phase. A Rietveld refinement is included at the lowest pressure environment to support this statement. The small residuals and R-values obtained in the refinement (Fig. 3) confirm that we succeed in the data analysis. Similar quality refinements were obtained at all pressures. In the HP experiments we have detected the presence of a minor amount of unreacted Yb_2O_3, which however did not preclude the determination of the crystal structure of $YbSbO_4$ at any pressure. This finding is consistent with EDX experiments, which determined a slightly excess of Yb in the sample composition. As can be observed in Fig. 3, with increasing pressure, XRD peaks gradually shift towards higher angles, due to the decrease of unit-cell parameters. We did not observe any evidence of the occurrence of a phase transition. However, a gradual merging of some of the peaks occurs, caused by the slightly anisotropic compressibility, as explained in the paragraph where axial compressibility is discussed.

From the Rietveld refinements of the experimental patterns, we have obtained the pressure dependence of the unit-cell parameters. The refinements were performed subsequently from the lowest to the highest pressure assuming the values obtained at a given pressure as the starting values for the next pressure. In the refinements the Bragg peak profiles were modelled using a pseudo-Voigt function. The occupancy and the overall atomic displacement factors were constrained to 1 and $B = 0.025$ $Å^2$, respectively, a typical approach used in DAC XRD experiments where the angular aperture is limited.[36] In a first step we fitted the lattice parameters (keeping atomic positions fixed). This was followed by the refinement of atomic positions (keeping lattice parameters fixed). To allow an estimation of the validity of our analysis, in Table 2 we present the lattice parameters and the R-values of the refinements corresponding to the pressures of the six XRD patterns shown in Fig. 3. The pressure dependence of unit-cell parameters is presented in Fig. 4. In the figure, it can be seen a good agreement between experiments and calculations. Computer simulations slightly overestimate the lattice parameters a, b, and c and slightly the parameter β ($a = 7.55677(2)$ Å, $b = 5.29890(1)$ Å, $c = 7.44748(2)$ Å, and $\beta = 98.15606(3)°$; for a comparison with experiments, see Table 1). The volume is overestimated by 1.5% by DFT simulations. This difference is typical of DFT calculations performed within the GGA approximation and it is related to the approximation used to describe the exchange–correlation energy.[37] Notice that the results of our DFT calculations agree
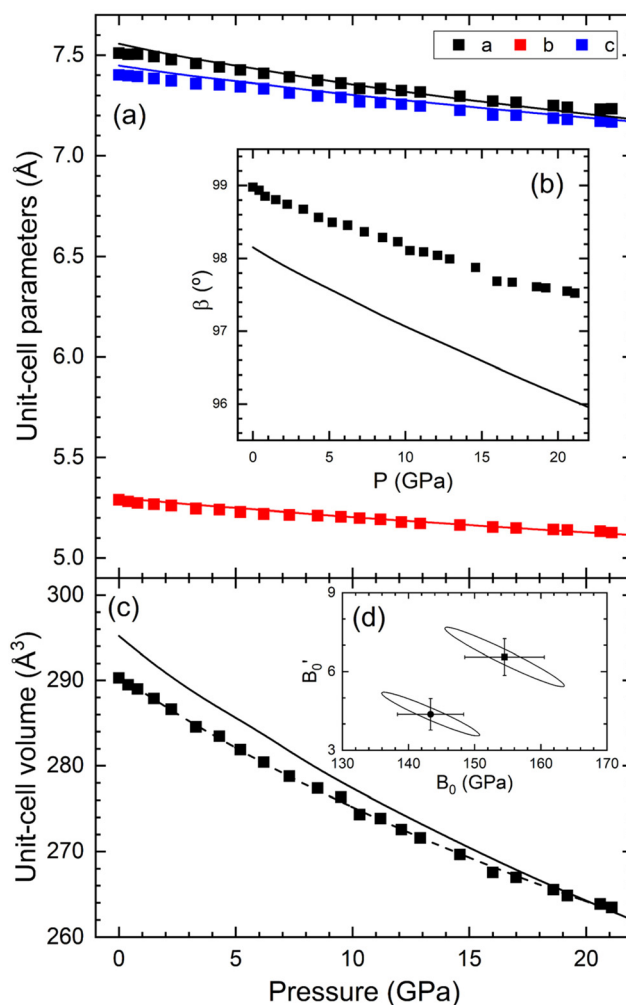

Fig. 4 Pressure dependence of (a) unit-cell parameters a, b, and c; (b) lattice parameter β; and (c) unit-cell volume. Symbols (solid lines) are results from experiments (calculations). The dashed line in (c) is the EoS fitting of experiments. (d) B'_0 versus B_0 including the one-sigma confidence ellipse of fit to results from experiments (square) and calculations (circle). When not shown errors are smaller than symbols.

better with experiments than those of DFT calculations reported in the Materials Project[38] ($a = 7.42$ Å, $b = 5.14$ Å, $c = 7.86$ Å, and $\beta = 98.00°$) which overestimate the unit-cell volume by 2.5% and the lattice parameter c by 5%.

Fig. 4(a) shows that the lattice parameter a is more compressible than the lattice parameter c, both becoming nearly identical at the maximum pressure covered by experiments. On the other hand, the lattice parameter β also decreases under compression (see Fig. 4(b)). Regarding the pressure dependence of the volume (see Fig. 4(c)), we have found that it can be described by a third-order Birch–Murnaghan equation of state (BM EoS).[39] According to the fits, the experimental unit-cell volume at zero pressure, bulk modulus, and its pressure derivative are $V_0 = 290.5(2)$ $Å^3$, $B_0 = 155(6)$ GPa, and $B'_0 = 6.6(7)$, respectively, while the corresponding theoretical values are $V_0 = 294.8(2)$ $Å^3$, $B_0 = 143(5)$ GPa and $B'_0 = 4.4(6)$. The

Table 2 Lattice parameters obtained from the Rietveld refinement of X-ray diffraction patterns for $YbSbO_4$ at different pressures. R-values of the refinements are included

P (GPa)	a (Å)	b (Å)	c (Å)	β (°)	R_P (%)	R_{WP} (%)
0.4	7.5032	5.28	7.397	98.9347	2.88	7.07
3.3	7.4583	5.245	7.358	98.6739	2.97	7.63
6.2	7.4088	5.218	7.3335	98.4561	3.13	8.20
10.3	7.3349	5.198	7.2677	98.11	3.29	8.76
16.0	7.2721	5.1542	7.2028	97.6861	3.45	9.16
21.1	7.233	5.1261	7.167	97.5246	3.52	9.22

compressibility given by calculations is slightly higher than the one obtained by the fits performed on the experimental data, because of the overestimation of the unit-cell volume at zero pressure by calculations.[37] The slightly larger compressibility obtained from calculations can be concluded from the one-sigma confidence ellipses of the B'_0 versus B_0 plot shown in Fig. 4(d). We have also analysed the changes induced by pressure in the unit-cell parameters. In a monoclinic structure, the compressibility tensor is not diagonal in the setting defined by the unit cell. Thus, the compressibility should be described by the eigenvalues and eigenvectors of the isothermal compressibility tensor.[40] In YbSbO$_4$, the main axes of compressibility are [$\bar{9}08$], [010], and [809], and their corresponding compressibilities are 2.4(1) 10^{-3} GPa^{-1}, 2.0(1) 10^{-3} GPa^{-1}, and 1.1(1) 10^{-3} GPa^{-1}, respectively. Thus, the most and least compressible axes are in the plane perpendicular to the unique axis of the structure. Notice that [$\bar{9}08$] and [809] form and angle of 3.4° with [$\bar{1}01$] and [101], respectively, which for practical reasons can be considered the most and least compressible axis. Their compressibilities slightly change to 2.38 (10) 10^{-3} GPa^{-1} and 1.08(10) 10^{-3} GPa^{-1}, respectively, which agree within errors with the compressibilities along [$\bar{9}08$] and [809].

From the Rietveld refinements of the XRD patterns, we have obtained the experimental pressure dependence of bond distances. In Fig. 5 we present the pressure dependence of the average Sb–O and Yb–O bond distances, the distortion index (DIndex) of the bonds, and the effective coordination number (ECN). These parameters were calculated using VESTA[41] (definitions can be found in the VESTA manual). In the figure, it is observed the change induced by pressure in Sb–O and Yb–O distances is comparable. Both distances are reduced approximately a 10% from 0.1 MPa to 20 GPa. Therefore, both the SbO$_6$ and YbO$_8$ polyhedra contribute to the volume change under compression. Indeed, using a 2nd order BM EoS a bulk modulus of 165(6) GPa is determined for YbO$_8$ and a bulk modulus of 162(6) GPa is determined for SbO$_6$. Both bulk moduli agree within error bars with the experimental bulk modulus of YbSbO$_4$, 155(6) GPa. This result is unusual for MTO$_4$ bimetal oxides, where usually the polyhedra of the smaller cation is less compressible than the polyhedra of the larger cation.[1] The similar compressibility of both polyhedra suggest that there could be a charge transfer between Yb^{3+} and Sb^{5+}, which could be mediated by oxygen atoms.[42] Such phenomenon has been found before in antimony oxides is often called "valence skipping".[42] Such phenomenon could promote Cooper pairing and hence superconductivity, a fact that deserves to be studied in future experiments combining low-temperature and high-pressure. We also found that the SbO$_6$ octahedron is basically not distorted by pressure, because DIndex changes little from 0 to 20 GPa. In contrast, the distortion of the YbO$_8$ polyhedron is reduced as pressure increases, as shown in Fig. 5. Another difference between the effect of pressure in both polyhedra is that the ECN is not affected by pressure for Sb. However, it increases with pressure for Yb.
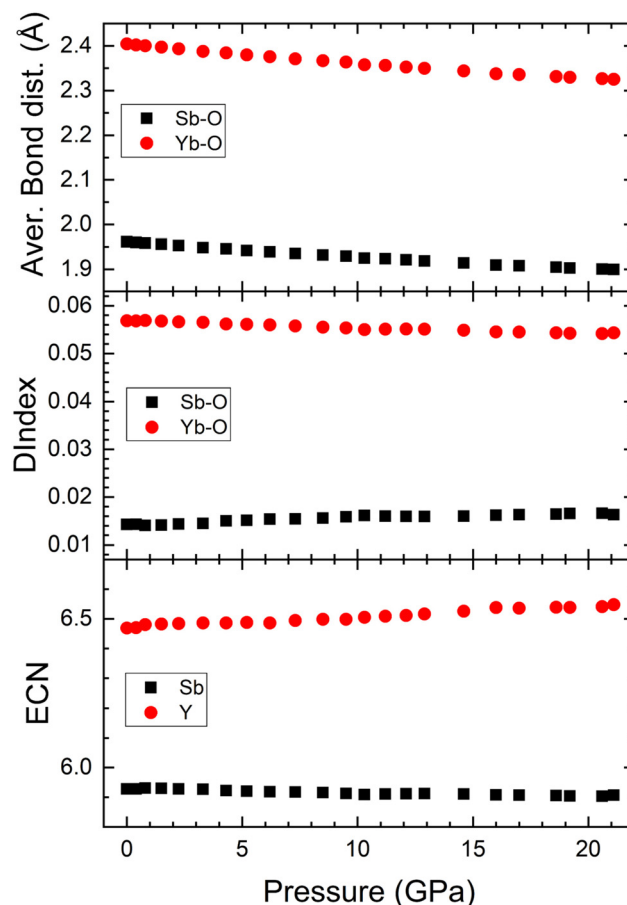

Fig. 5 Pressure dependence of the average bond distances, the distortion index (DIndex), and the effective coordination number (ECN).

We will now compare the behaviour of YbSbO$_4$ with other antimony oxides. YbSbO$_4$ has found a large structural stability as BiSbO$_4$.[17] Not only that, but their bulk moduli are also similar, 155(6) GPa in YbSbO$_4$ and 149(6) GPa in BiSbO$_4$.[17] However, this behaviour contrasts with Sb$_2$O$_3$[43] and SbPO$_4$.[44] Sb$_2$O$_3$ undergoes phase transitions at 3.5 and 10 GPa, and it is highly compressible with a bulk modulus of 20(2) GPa.[43] SbPO$_4$ experiences a transition at 9 GPa and is also highly compressible, $B_0 = 36(3)$.[44] The notorious difference in the behaviours is related to the different activity of the lone-electron pair (LEP) of Sb. In Sb$_2$O$_3$ and SbPO$_4$, Sb atoms are 4-fold coordinated to O in a trigonal–bipyramidal fashion. The distortion of the Sb polyhedron is caused by the strong LEP, which points to the opposite direction of the base of the pyramid. This fact favours compressibility and triggers structural instabilities causing phase transitions at low pressure. In the case of YbSbO$_4$ and BiSbO$_4$, the LEP is not active, and Sb is 6-fold coordinated, resembling the coordination polyhedron of a platonic octahedron, making the structure extremely stable and with a compressibility comparable to that of lanthanide phosphates and smaller than that of vanadates and most MTO$_4$ bimetal oxides.[45,46] Given the structural similitudes between YbSbO$_4$ and the rest of lanthanide antimonates, we

can foresee that all these compounds will have a similar pressure stability than $YbSbO_4$ and similar mechanical properties.

DFT calculations agree with experiments regarding the changes induced by pressure in the crystal structure and confirm the dynamical and mechanical stability of the low-pressure phase. Table 3 shows the calculated elastic constants. The obtained constants fulfil the generalized Born criteria,[47] confirming that the structure of $YbSbO_4$ is mechanically stable. From the elastic constants, we have calculated the elastic moduli within the Hill approximation.[48] The obtained bulk modulus, 148.33 GPa, agrees with the values obtained from experiments and total-energy calculations. The Young modulus, $E = 124.14$ GPa, is comparable to the bulk modulus, but the shear modulus, $G = 45.62$ GPa, is considerably smaller. Thus, elastic constant calculations confirm that $YbSbO_4$ is a non-compressible material with a large tensile (or compressive) stiffness when a force is applied lengthwise. On the other hand, shear deformations are favoured over volume contraction, making $YbSbO_4$ susceptible to large non-hydrostatic stresses.[49] In addition, according to the calculated Vickers Harness (H_V) and the B/G ratio (>1.75), we can postulate that $YbSbO_4$ is probably a ductile material.[50] Notice that according to our DFT calculations the Poisson ratio is $\nu = 0.361$, being this result consistent with the hypothesis that $YbSbO_4$ is a ductile material. However, this fact needs confirmation from single crystal measurements.[51]

The calculated phonon dispersion and phonon density of states at different pressures are shown in Fig. 6. The phonon dispersion shows that there are no imaginary phonon branches in the pressure range of this study. This supports the dynamical stability of $YbSbO_4$. We have also calculated the phonon frequencies and their pressure dependence for Raman-active and infrared (IR)-active modes. The results are summarized in Table 4, where they are compared with previous Raman experiments.[18] The agreement for Raman frequencies at ambient pressure is quite good. Therefore, our calculations can be used for mode assignment and for validation of future HP Raman and IR experiments. Using group theory,

Table 3 Calculated elastic constants C_{ij} for $YbSbO_4$ at ambient pressure. The bulk (B), shear (G), and Young (E) moduli, Poisson ratio (n), B/G ratio, and Hardness (H_V) are also included

C_{ij} (GPa)		Property	
C_{11}	229.01	B (GPa)	148.33
C_{22}	282.52	G (GPa)	45.62
C_{33}	270.88	E (GPa)	124.14
C_{44}	89.59	ν	0.361
C_{55}	64.26	B/G	3.251
C_{66}	7.40	H_v (GPa)	3.600
C_{12}	101.00		
C_{13}	86.98		
C_{15}	18.38		
C_{23}	96.65		
C_{25}	15.71		
C_{35}	0.44		
C_{46}	−1.08		
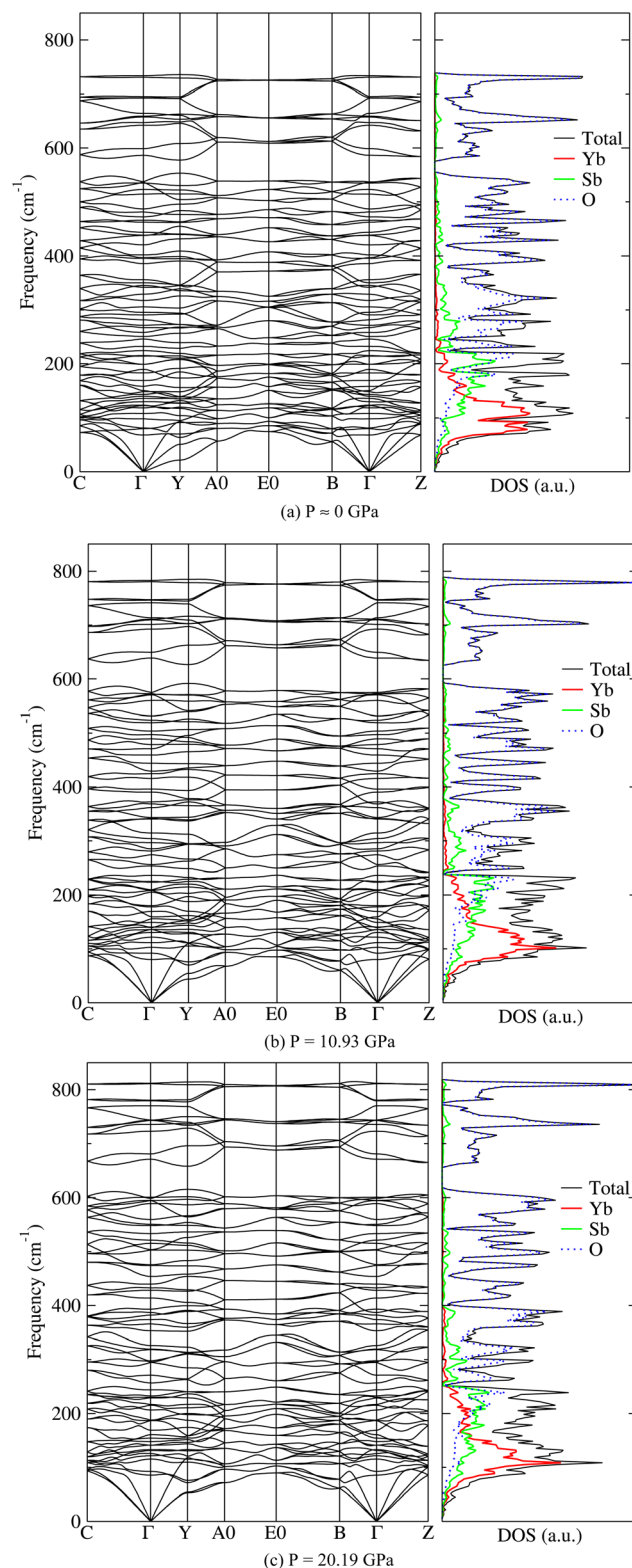
Fig. 6 Phonon dispersion and Phonon Density of States (PDOS) of $YbSbO_4$ at different pressures. (a) 0 GPa, (b) 10.93 GPa, and (c) 20.19 GPa.

the following 72 vibrational modes are predicted at the Γ point of the BZ; $\Gamma = 18A_g + 18B_g + 18A_u + 18B_u$. Among them, $A_u + 2B_u$ are the acoustic modes. The rest of the modes are all

Table 4 Calculated optical phonon frequencies ω (in cm^{-1}) at the Γ point, pressure coefficients dω/dP (in cm^{-1} GPa^{-1}), and Grüneisen parameter γ for YbSbO$_4$ at ambient pressure. Raman results are compared with previous experiments (ω_{exp})[18]

	Raman				IR			
Mode	ω_{exp}	ω	dω/dP	γ	Mode	ω	dω/dP	γ
B$_g$	70	68.25	0.893	2.115	A$_u$	78.56	1.832	3.467
A$_g$	82	80.66	0.546	1.167	B$_u$	117.79	0.722	1.058
A$_g$	96	97.74	1.267	2.094	B$_u$	129.70	0.933	1.221
B$_g$	105	108.01	1.176	1.783	A$_u$	134.57	−0.390	−0.490
A$_g$	113	122.59	1.024	1.405	B$_u$	142.04	2.266	2.511
B$_g$	117	123.83	0.901	1.236	A$_u$	149.71	1.023	1.160
A$_g$	124	138.90	0.768	0.954	A$_u$	167.69	0.950	0.974
A$_g$	130	147.91	0.646	0.759	A$_u$	197.91	0.960	0.836
B$_g$	147	157.75	1.505	1.585	B$_u$	198.15	0.437	0.405
B$_g$	161	181.23	2.434	2.157	B$_u$	211.99	1.084	0.878
A$_g$	173	187.84	1.378	1.239	A$_u$	212.96	0.899	0.733
B$_g$	200	222.36	1.089	0.846	B$_u$	248.72	0.508	0.362
A$_g$		229.74	2.067	1.495	A$_u$	257.66	2.079	1.354
B$_g$	242	245.11	2.553	1.714	B$_u$	269.17	1.345	0.861
A$_g$	252	264.90	2.713	1.686	B$_u$	288.01	4.270	2.353
B$_g$	272	279.47	2.009	1.216	A$_u$	294.55	1.577	0.923
A$_g$	292	315.30	2.130	1.151	A$_u$	303.46	3.143	1.706
B$_g$	312	326.54	2.794	1.432	B$_u$	339.58	2.406	1.199
A$_g$		342.89	2.561	1.258	A$_u$	384.52	2.353	1.046
A$_g$	328	349.13	4.035	1.884	A$_u$	394.83	3.020	1.290
B$_g$	336	353.76	3.122	1.471	B$_u$	418.64	2.736	1.118
A$_g$	357	393.16	4.125	1.726	B$_u$	435.69	3.479	1.339
B$_g$	385	399.93	2.057	0.886	A$_u$	442.36	3.942	1.485
B$_g$	410	436.36	3.348	1.295	A$_u$	470.32	3.898	1.391
B$_g$		459.81	3.658	1.337	B$_u$	484.69	3.729	1.298
A$_g$	465	463.74	2.578	0.955	B$_u$	532.49	3.087	0.994
A$_g$		479.39	3.617	1.274	A$_u$	533.56	3.239	1.039
A$_g$	501	511.58	3.890	1.283	A$_u$	597.41	4.154	1.181
B$_g$		520.02	3.784	1.234	B$_u$	641.11	4.119	1.097
B$_g$	530	535.43	3.227	1.028	A$_u$	656.05	4.326	1.123
B$_g$	557	584.80	4.306	1.246	B$_u$	691.25	3.914	0.973
A$_g$	570	645.65	4.463	1.174	B$_u$	693.28	4.335	1.069
B$_g$		658.22	4.259	1.104	A$_u$	731.58	3.967	0.934
A$_g$	665	663.16	4.104	1.058				
A$_g$	719	691.90	4.334	1.070				
B$_g$	746	729.44	4.046	0.954				

optical modes. Among them, 36 are Raman-active modes (18A$_g$ + 18B$_g$), and 33 are IR-active modes (17A$_u$ + 16B$_u$). As shown in Table 4, one IR A$_u$ mode (ω = 134.57 cm^{-1}) softens with pressure, while the other IR and Raman modes harden under compression with pressure coefficients comparable to those of BiSbO$_4$.[17] All modes have Grüneisen parameters between 0.8 and 1.8 with only few exceptions, like the lowest-frequency Raman-active B$_g$ mode and the lowest-frequency IR-active A$_u$ mode. In addition, there is an IR-active Au mode with a negative pressure Grüneisen parameter. The existence of a mode that gradually softens under compression suggests that structural instabilities may arise at pressures higher than covered by this work.[52]

From the phonon density of states (see Fig. 6), we can see that high-frequency modes correspond to vibrations of oxygen atoms. In particular, the modes with frequencies higher than 590 cm^{-1} are mainly due to internal stretching vibrations of the SbO$_6$ octahedron. The modes with frequencies between 430 and 560 cm^{-1} are associated to bending vibrations of the same octahedron. The rest of the modes correspond to

vibrations involving Yb atoms and SbO$_6$ octahedra movements as rigid units.

4. Conclusions

By means of high-pressure X-ray diffraction experiments and density functional theory calculations we have found that, similarly to BiSbO$_4$, YbSbO$_4$ does not undergo any phase transition in the pressure range covered by this study. This behaviour is very different from that of other antimony oxides which undergo phase transition below 10 GPa. The difference in the high-pressure behaviour is related to the inactive lone electron pair in YbSbO$_4$. It has also been found that YbSbO$_4$ is among the least compressible MTO$_4$ bimetallic oxides, which could be probably related to a charge transfer between cations. Calculations also provide information on the elastic constants, phonon frequencies and their pressure dependence, which could be relevant for applications of YbSbO$_4$. The possibility of

the occurrence of charge transfer between cations is also discussed.

Author contributions

Alka B. Garg: Conceptualization, formal analysis, investigation, writing – review & editing, Sinhue Lopez-Moreno: Investigation, methodology, writing – review & editing, Pablo Botella-Vives: Investigation, Oscar Gomis: Investigation, Enrico Bandiello: Investigation, Hussien Osman: Investigation, Catalin Popescu: Investigation, Daniel Errandonea: Conceptualization, formal analysis, funding acquisition, investigation, project administration, writing – original draft, writing – review & editing.

Conflicts of interest

The authors declare that they have no known competing financial interests or personal relationships that could have appeared to influence the work reported in this paper.

Acknowledgements

References

1 D. Errandonea and F. J. Manjon, Pressure effects on the structural and electronic properties of ABX$_4$ scintillating crystals, *Prog. Mater. Sci.*, 2008, **53**, 711–773, DOI: 10.1016/j.pmatsci.2008.02.001.

2 D. Errandonea and A. B. Garg, Recent progress on the characterization of the high-pressure behaviour of AVO$_4$ orthovanadates, *Prog. Mater. Sci.*, 2018, **97**, 123–169, DOI: 10.1016/j.pmatsci.2018.04.004.

3 R. Lacomba-Perales, D. Errandonea, Y. Meng and M. Bettinelli, High-pressure stability and compressibility of APO$_4$ (A = La, Nd, Eu, Gd, Er, and Y) orthophosphates: An X-ray diffraction study using synchrotron radiation, *Phys. Rev. B: Condens. Matter Mater. Phys.*, 2010, **81**, 064113, DOI: 10.1103/PhysRevB.81.064113.

4 J. Sharma, H. Q. Afful and C. E. Packard, Phase Transformation Pathway of DyPO4 to 21.5 GPa, *Crystals*, 2023, **13**, 249, DOI: 10.3390/cryst13020249.

5 D. Errandonea, R. S. Kumar, S. N. Achary and A. K. Tyagi, In situ high-pressure synchrotron X-ray diffraction study of CeVO$_4$ and TbVO$_4$ up to 50 GPa, *Phys. Rev. B: Condens. Matter Mater. Phys.*, 2011, **84**, 224121, DOI: 10.1103/PhysRevB.84.224121.

6 B. Wang, K. Sun and G. Chu, Pressure-induced phase transitions in TmVO$_4$ investigated by Raman spectroscopy, *Spectrochim. Acta, Part A*, 2023, **286**, 121945, DOI: 10.1016/j.saa.2022.121945.

7 D. Errandonea, F. Rodriguez, R. Vilaplana, D. Vie, S. Garg, B. Nayak, N. Garg, J. Singh, V. Kanchana and G. Vaitheeswaran, Band-Gap Energy and Electronic d–d Transitions of NiWO$_4$ Studied under High-Pressure Conditions, *J. Phys. Chem. C*, 2023, **127**, 15630–15640, DOI: 10.1021/acs.jpcc.3c03512.

8 M. Ye, Y. Zhou, T. Shao, H. Liu, Q. Tao, X. Wang, R. Tang, H. Yue, Y. Li and P. Zhu, Effects of High Pressure on the Bandgap and the d–d Crystal Field Transitions in Wolframite NiWO$_4$, *J. Phys. Chem. C*, 2023, **127**, 6543–6551, DOI: 10.1021/acs.jpcc.2c09036.

9 D. Errandonea, L. Gracia, R. Lacomba-Perales, A. Polian and J. C. Chervin, Compression of scheelite-type SrMoO$_4$ under quasi-hydrostatic conditions: Redefining the high-pressure structural sequence, *J. Appl. Phys.*, 2013, **113**, 123510, DOI: 10.1063/1.4798374.

10 V. Panchal, C. Popescu and D. Errandonea, An Investigation of the Pressure-Induced Structural Phase Transition of Nanocrystalline α-CuMoO$_4$, *Crystals*, 2022, **12**, 365, DOI: 10.3390/cryst12030365.

11 E. Bandiello, D. Errandonea, D. Martinez-Garcia, D. Santamaria-Perez and F. J. Manjón, Effects of high-pressure on the structural, vibrational, and electronic properties of monazite-type PbCrO$_4$, *Phys. Rev. B: Condens. Matter Mater. Phys.*, 2012, **85**, 024108, DOI: 10.1103/PhysRevB.85.024108.

12 D. Santamaría-Pérez, R. S. Kumar, A. J. Dos Santos-García, D. Errandonea, R. Chuliá-Jordán, R. Saez-Puche,

P. Rodríguez-Hernández and A. Muñoz, High-pressure transition to the post-barite phase in BaCrO₄ hashemite, *Phys. Rev. B: Condens. Matter Mater. Phys.*, 2012, **86**, 094116, DOI: **10.1103/PhysRevB.86.094116**.

13 A. B. Garg, A. Liang, D. Errandonea, P. Rodríguez-Hernández and A. Muñoz, Monoclinic–triclinic phase transition induced by pressure in fergusonite-type YbNbO₄, *J. Phys.: Condens. Matter*, 2022, **34**, 174007, DOI: **10.1088/1361-648X/ac5202**.

14 T. Ouahrani, A. B. Garg, R. Rao, P. Rodríguez-Hernández, A. Muñoz, M. Badawi and D. Errandonea, High-Pressure Properties of Wolframite-Type ScNbO₄, *J. Phys. Chem. C*, 2022, **126**, 4664–4676, DOI: **10.1021/acs.jpcc.1c10483**.

15 S. Banerjee, A. Tyagi and A. B. Garg, Pressure-Induced Monoclinic to Tetragonal Phase Transition in RTaO₄ (R = Nd, Sm): DFT-Based First Principles Studies, *Crystals*, 2023, **13**, 254, DOI: **10.3390/cryst13020254**.

16 S. Banerjee, A. B. Garg and H. K. Poswal, Structural and vibrational properties of GdTaO₄ under compression: An insight from experiment and first principles simulations, *J. Appl. Phys.*, 2023, **133**, 025902, DOI: **10.1063/5.0132944**.

17 D. Errandonea, A. Muñoz, P. Rodríguez-Hernández, O. Gomis, S. N. Achary, C. Popescu, S. J. Patwe and A. K. Tyagi, High-Pressure Crystal Structure, Lattice Vibrations, and Band Structure of BiSbO₄, *Inorg. Chem.*, 2016, **55**, 4958–4969, DOI: **10.1021/acs.inorgchem**.

18 K. P. F. Siqueira, P. P. Lima, R. A. S. Ferreira, L. D. Carlos, E. M. Bittar, E. Granado, J. C. Gonzalez, A. Abelenda, R. L. Moreira and A. Dias, Lanthanide Orthoantimonate Light Emitters: Structural, Vibrational, and Optical Properties, *Chem. Mater.*, 2014, **26**, 6351–6360, DOI: **10.1021/cm502504b**.

19 A. Liang, R. Turnbull and D. Errandonea, A review on the advancements in the characterization of the high-pressure properties of iodates, *Prog. Mater. Sci.*, 2023, **136**, 101092, DOI: **10.1016/j.pmatsci.2023.101092**.

20 H. K. Mao, X. J. Chen, Y. Ding, B. Li and L. Wang, Solids, liquids, and gases under high pressure, *Rev. Mod. Phys.*, 2018, **90**, 015007, DOI: **10.1103/RevModPhys.90.015007**.

21 F. Fauth, I. Peral, C. Popescu and M. Knapp, The new material science powder diffraction beamline at ALBA synchrotron, *Powder Diffr.*, 2013, **28**, S360–S370, DOI: **10.1017/S0885715613000900**.

22 S. Klotz, J. C. Chervin, P. Munsch and G. Le Marchand, Hydrostatic limits of 11 pressure transmitting media, *J. Phys. D: Appl. Phys.*, 2009, **42**, 075413, DOI: **10.1088/0022-3727/42/7/075413**.

23 A. Dewaele, P. Loubeyre and M. Mezouar, Equations of state of six metals above 94 GPa, *Phys. Rev. B: Condens. Matter Mater. Phys.*, 2004, **70**, 094112, DOI: **10.1103/PhysRevB.70.094112**.

24 C. Prescher and V. B. Prakapenka, DIOPTAS: a program for reduction of two-dimensional X-ray diffraction data and data exploration, *High Pressure Res.*, 2015, **35**, 223–230, DOI: **10.1080/08957959.2015.1059835**.

25 J. Rodríguez-Carvajal, Recent advances in magnetic structure determination by neutron powder diffraction, *Phys. B*, 1993, **192**, 55–69, DOI: **10.1016/0921-4526(93)90108-I**.

26 R. O. Jones, Density functional theory: Its origins, rise to prominence, and future, *Rev. Mod. Phys.*, 2915, **87**, 897–923, DOI: **10.1103/RevModPhys.87.897**.

27 P. E. Blöchl, Projector augmented-wave method, *Phys. Rev. B: Condens. Matter Mater. Phys.*, 1994, **50**, 17953–17979, DOI: **10.1103/PhysRevB.50.17953**.

28 G. Kresse and D. Joubert, From ultrasoft pseudopotentials to the projector augmented-wave method, *Phys. Rev. B: Condens. Matter Mater. Phys.*, 1999, **59**, 1758–1775, DOI: **10.1103/PhysRevB.59.1758**.

29 G. Kresse and J. Furthmüller, Efficient iterative schemes for ab initio total-energy calculations using a plane-wave basis set, *Phys. Rev. B: Condens. Matter Mater. Phys.*, 1996, **54**, 11169–11186, DOI: **10.1103/PhysRevB.54.11169**.

30 G. I. Csonka, J. P. Perdew, A. Ruzsinszky, P. H. T. Philipsen, S. Lebègue, J. Paier, O. A. Vydrov and J. G. Ángyán, Assessing the performance of recent density functionals for bulk solids, *Phys. Rev. B: Condens. Matter Mater. Phys.*, 2009, **79**, 155107, DOI: **10.1103/PhysRevB.79.155107**.

31 H. J. Monkhorst and J. D. Pack, Special points for Brillouin-zone integrations, *Phys. Rev. B: Solid State*, 1976, **13**, 5188–5192, DOI: **10.1103/PhysRevB.13.5188**.

32 K. Parlinski, *Computer Code PHONON*, **https://wolf.ifj.edu.pl/phonon**, 2008.

33 Y. Le Page and P. Saxe, Symmetry-general least-squares extraction of elastic data for strained materials from ab initio calculations of stress, *Phys. Rev. B: Condens. Matter Mater. Phys.*, 2002, **65**, 104104, DOI: **10.1103/PhysRevB.65.104104**.

34 N. A. Asryan, A. S. Alikhanyan and G. D. Nipan, Specifics of Sublimation of Antimony Oxides, *Dokl. Phys. Chem.*, 2003, **392**, 221–226, DOI: **10.1023/A:1025776803970**.

35 S. Gerlach, R. Cardoso-Gil, E. Milke and M. Schmidt, Chemical vapour transport and crystal structure of rare-rarth antimonates(V) - RESbO₄, *Z. Anorg. Allg. Chem.*, 2007, **633**, 83–92, DOI: **10.1002/zaac.200600249**.

36 D. Errandonea, R. S. Kumar, O. Gomis, F. J. Manjón, V. V. Ursaki and I. M. Tiginyanu, X-ray diffraction study on pressure-induced phase transformations and the equation of state of ZnGa₂Te₄, *J. Appl. Phys.*, 2013, **114**, 233507, DOI: **10.1063/1.4851735**.

37 K. Lejaeghere, L. Vanduyfhuys, T. Verstraelen, V. Van Speybroeck and S. Cottenier, Is the error on first-principles volume predictions absolute or relative?, *Comput. Mater. Sci.*, 2016, **117**, 390–396, DOI: **10.1016/j.commatsci.2016.01.039**.

38 See **https://next-gen.materialsproject.org/materials/mp-1237084**.

39 F. Birch, Finite elastic strain of cubic crystals, *Phys. Rev.*, 1947, **71**, 809–824, DOI: **10.1103/PhysRev.71.809**.

40 K. S. Knight, Analytical expressions to determine the isothermal compressibility tensor and the isobaric thermal expansion tensor for monoclinic crystals: Application to determine the direction of maximum compressibility in Jadeite, *Phys. Chem. Miner.*, 2010, **37**, 529–533, DOI: **10.1007/s00269-009-0353-8**.

41 K. Momma and F. Izumi, VESTA 3 for three-dimensional visualization of crystal, volumetric and morphology data, *J. Appl. Crystallogr.*, 2011, **44**, 1272–1276, DOI: **10.1107/S0021889811038970**.

42 M. Kim, G. M. McNally, H. H. Kim, *et al.*, Superconductivity in (Ba,K)SbO$_3$, *Nat. Mater.*, 2022, **21**, 627–633, DOI: **10.1038/s41563-022-01203-7**.

43 A. L. J. Pereira, L. Gracia, D. Santamaría-Pérez, R. Vilaplana, F. J. Manjón, D. Errandonea, M. Nalin and A. Beltran, Structural and vibrational study of cubic Sb$_2$O$_3$ under high pressure, *Phys. Rev. B: Condens. Matter Mater. Phys.*, 2012, **85**, 174108, DOI: **10.1103/PhysRevB.85.174108**.

44 A. L. J. Pereira, D. Santamaría-Pérez, R. Vilaplana, D. Errandonea, C. Popescu, E. L. da Silva, J. A. Sans, J. Rodríguez-Carvajal, A. Muñoz, P. Rodríguez-Hernández, A. Mujica, S. E. Radescu, A. Beltrán, A. Otero-de-la-Roza, M. Nalin, M. Mollar and F. J. Manjón, Experimental and Theoretical Study of SbPO$_4$ under Compression, *Inorg. Chem.*, 2020, **59**, 287–307, DOI: **10.1021/acs.inorgchem.9b02268**.

45 O. Gomis, B. Lavina, P. Rodríguez-Hernández, A. Muñoz, R. Errandonea, D. Errandonea and M. Bettinelli, High-pressure structural, elastic, and thermodynamic properties of zircon-type HoPO$_4$ and TmPO$_4$, *J. Phys.: Condens. Matter*, 2017, **29**, 095401, DOI: **10.1088/1361-648X/aa516a**.

46 D. Errandonea, High pressure crystal structures of orthovanadates and their properties, *J. Appl. Phys.*, 2020, **128**, 040903, DOI: **10.1063/5.0016323**.

47 G. Grimvall, B. Magyari-Köpe, V. Ozoliņš and K. A. Persson, Lattice instabilities in metallic elements, *Rev. Mod. Phys.*, 2012, **84**, 945–986, DOI: **10.1103/RevModPhys.84.945**.

48 R. Hill, The elastic behaviour of a crystalline aggregate, *Proc. Phys. Soc., London, Sect. A*, 1952, **65**, 349–354, DOI: **10.1088/0370-1298/65/5/307**.

49 D. Errandonea, A. Muñoz and J. Gonzalez-Platas, Comment on "High-pressure X-ray diffraction study of YBO$_3$/Eu^{3+}, GdBO$_3$, and EuBO$_3$: Pressure-induced amorphization in GdBO$_3$" [J. Appl. Phys. 115, 043507 (2014)], *J. Appl. Phys.*, 2014, **115**, 216101, DOI: **10.1063/1.4881057**.

50 S. F. Pugh, Relations between the elastic moduli and the plastic properties of polycrystalline pure metals, *Philos. Mag.*, 1954, **45**, 823–843, DOI: **10.1080/14786440808520496**.

51 S. Kise, Y. Araki, T. Omori and R. Kainuma, Orientation Dependence of Plasticity and Fracture in Single-Crystal Superelastic Cu-Al-Mn SMA Bars, *J. Mater. Civ. Eng.*, 2021, **33**, 4, DOI: **10.1061/(ASCE)MT.1943-5533.0003568**.

52 A. Liang, S. Rahman, P. Rodriguez-Hernandez, A. Muñoz, F. J. Manjón, G. Nenert and D. Errandonea, High-pressure Raman study of Fe(IO$_3$)$_3$: Soft-mode behavior driven by coordination changes of iodine atoms, *J. Phys. Chem. C*, 2020, **124**, 21329–21337, DOI: **10.1021/acs.jpcc.0c06541**.